*Composites: Science and Technology, in press (2016)*

# Measuring and Modeling Fiber Bridging: Application to Wood and Wood Composites Exposed to Moisture Cycling

B. Mirzaei, A. Sinha, and J.A. Nairn

*Wood Science and Engineering, Oregon State University, Corvallis, OR 97330, USA*

*Submitted 30 Nov 2015, Revised 1 Mar 2016*

**Abstract**

We propose a new method for determining fiber-bridging, cohesive laws in fiber-reinforced composites and in natural fibrous materials. In brief, the method requires direct measurement of energy released during crack growth, known as the *R* curve, followed by a new approach to extracting a cohesive law. We claim that some previous attempts at determining cohesive laws have used inappropriate, and potentially inaccurate, methods. This new approach was applied to finding fiber bridging tractions in laminated veneer lumber (LVL) made from Douglas-fir veneer and four different adhesives. In addition, the LVL specimens were subjected to moisture exposure cycles and observations of changes in the bridging cohesive laws were used to rank the adhesives for their durability. Finally, we developed both analytical and numerical models for fiber bridging materials. The numerical modeling was a material point method (MPM) simulation of crack propagation that includes crack tip propagation, fiber bridging zone development, and steady state crack growth. The simulated *R* curves agreed with experimental results.

*K*eywords: Wood, Durability, Fracture toughness, Computational mechanics, Fibre bridging

## 1. Introduction

Many materials develop process zones in the wake of crack tip propagation including both synthetic composites [1, 2] and natural materials such as bone [3], wood [4–6], or wood composites [7–9]. For both fiber-reinforced composites and fiber-based natural materials, a common type of process zone is a fiber bridging zone. Such zones can be a significant component of a material's toughness because the zone size can be comparable to, or larger than, the specimen size [8]. One way to guide interpretation of experiments or to design structures that use fiber bridging materials is to model the process zone with a cohesive law that gives crack surface tractions as a function of crack opening displacement. The practical use of such laws, however, requires methods to measure them. This paper describes a new approach to measuring cohesive laws with application to wood and wood composites. The measured laws were used to characterize materials and were implemented in a numerical model to validate their role in modeling crack propagation.

A key concept for understanding crack propagation in the presence of a process zone is that there are two crack tips — the actual "crack tip" at the leading edge of the process zone and the "notch root" at its trailing edge (see Fig. 1A). When a crack propagation experiment begins, the crack tip and notch root coincide at the "initial" crack tip. When loading causes energy release rate for crack tip growth to exceed the initiation toughness, the crack tip propagates, but the notch root does not. Instead, a "developing" process zone is left in the wake of the crack tip that grows as the crack tip propagates. During this phase, the crack resistance, *R*, increases, which is known as the material's *R* curve. Eventually the crack opening displacement (COD) at the notch root, $\delta_{root}$, exceeds the critical COD for the process zone, $\delta_c$. After $\delta_c$ is reached, the crack tip and the notch root propagate together in a regime termed "steady state" crack growth. In steady state crack growth, *R* is constant at a plateau called the steady state toughness, $G_{ss}$. In brief, the material's *R* curve increases until the notch root starts to propagate and thereafter remains constant at $G_{ss}$.

Figure 1A shows a contour Γ from the bottom crack surface to the top surface that completely encloses the process zone. When part of the crack within the contour is connected by a bridging law, Bao and Suo [10] derived the *J* integral along the enclosing contour, called here the far-field *J* integral or $J_{ff}(\delta_{root})$, as:

$$J_{ff}(\delta_{root}) = J_{tip,c} + \int_0^{\delta_{root}} \sigma(\delta)\, d\delta \qquad (1)$$

where $\sigma(\delta)$ is a traction law associated with the process zone. But, as is known in *J*-integral analysis, this *J* is only equal to the energy release rate when the crack growth is "self similar" [11]. When a process zone is involved, self similarity implies that the process zone length is constant during crack growth and this condition only occurs in the steady

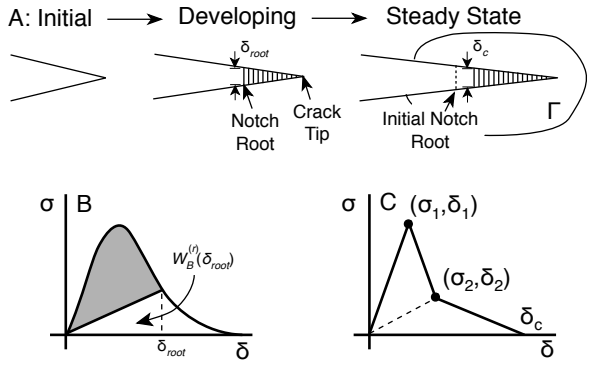


Figure 1: A. Stages of crack propagation in the presences of a process zone, which is defined by two crack tips — the actual crack tip and the notch root. B. Schematic drawing for a cohesive law. The shaded region is the energy dissipated in the zone and $W_B^{(r)}(\delta_{root})$ is the recoverable energy in the zone (shown here as elastic recovery, but other types of recovery could be modeled). C. A representation of fiber bridging tractions as a trilinear traction law derived for modeling purposes.

state regime with constant $R$. Prior to steady state, the energy required to propagate the crack needs to account for energy required both to propagate the crack tip and to enlarge the process zone. Nairn [12] has shown that in the region prior to steady state where the crack tip is propagating but the notch root is not, the increasing $R$ curve should be found not from $J_{ff}(\delta_{root})$, but rather from:

$$\begin{aligned} R(\delta_{root}) &= J_{ff}(\delta_{root}) - W_B^{(r)}(\delta_{root}) \\ &= J_{tip,c} + \int_0^{\delta_{root}} \sigma(\delta)\, d\delta - W_B^{(r)}(\delta_{root}) \end{aligned} \quad (2)$$

where $W_B^{(r)}(\delta_{root})$ is recoverable energy in the process zone, which is non-zero when $\delta_{root} < \delta_c$ . The amount of recoverable energy will depend on the mechanics of the process zone. A reasonable approximation for fiber bridging is that the process zone is an elastic zone undergoing damage such that recoverable energy is found by unloading back to the origin or $W_B^{(r)}(\delta_{root}) = \delta_{root}\sigma(\delta_{root})/2$ (see Fig. 1B) [12]. Stated differently, $J_{ff}(\delta_{root})$ is always the correct $J$ integral, but that single quantity cannot simultaneously give energy release rate both for process zone development (where crack tip propagates but notch root does not) and for steady-state crack growth (where crack tip and notch root propagate together as self-similar propagation). The solution is to use Eq. (2) to find the $R$ curve. This calculation of $R$ will differ from $J_{ff}(\delta_{root})$ during process zone development, but will equal it during steady-state crack growth.

Accepting the model that fracture with a fiber-bridging process zone can be modeled using fracture mechanics and a cohesive law, Eqs. (1) and (2) suggest three valid methods for determining $\sigma(\delta)$. The first is to measure $J_{ff}(\delta_{root})$ during process zone development and then differentiate to get:

$$\sigma(\delta) = \frac{dJ_{ff}(\delta_{root})}{d\delta_{root}} \quad (3)$$

Unfortunately, in general it is not possible to measure $J_{ff}(\delta_{root})$ from typical fracture specimens because the calculated result depends on the cohesive law. One exception, as pointed out by Rice [11], is a pure moment-loaded, double cantilever beam specimen. Lindhagen and Berglund [2] used such a specimen to measure cohesive laws in several glass mat composites with random in plane fiber orientation and observed monotonic softening behavior. Two drawbacks of this approach are that it requires special fixturing to apply a pure moment and it only works for one specimen geometry. This approach could never, for example, be used to probe important questions about potential changes in cohesive laws depending on specimen loading method. We also note that although $J_{ff}(\delta_{root})$, when it can be measured, can be used to find $\sigma(\delta)$, it cannot be used to measure the material's $R$ curve (if that is of interest). As seen in Eq. (2), the material's $R$ curve (*i.e.*,$R(\delta_{root})$) is not equal to $J_{ff}(\delta_{root})$ prior to steady state (because $W_B^{(r)}(\delta_{root}) > 0$ in that phase).

A second, valid approach is to avoid measurement of $J_{ff}(\delta_{root})$ or $R(\delta_{root})$ by directly measuring displacements in the arms of a double cantilever beam specimen and then numerically solving the inverse problem to find the traction law required such that the calculated and measured displacements agree. This approach was used by Botsis and coworkers [13–16]; they measured arm displacements using an embedded Fiber Bragg Grating (FBG) sensor and used finite element analysis to extract a cohesive law. The drawbacks of this approach are that specimens with FBGs are expensive and the technique is limited to synthetic composites where FBGs can be embedded during fabrication. The approach could not be used for studying fiber bridging in natural materials, such as solid wood. Vasic and Smith [17, 18] developed a similar method where cohesive law was found by numerically matching finite element predictions to crack opening displacements in wood measured in a scanning electron microscope.

A third option is to directly measure $R(\delta_{root})$ using energy tracking methods [4–9]. Differentiating this result using Eq. (2) and using an elastic approximation to $W_B(\delta_{root})$ (which is appropriate for fiber bridging), gives

$$\frac{dR(\delta_{root})}{d\delta_{root}} = \frac{1}{2}\left(\sigma(\delta_{root}) - \delta_{root}\frac{d\sigma(\delta_{root})}{d\delta_{root}}\right) \quad (4)$$

This differential equation can be solved for $\sigma(\delta_{root})$ to give a new approach for finding cohesive law from $R(\delta_{root})$ [12]:

$$\sigma(\delta_{root}) = 2\delta_{root}\int_{\delta_{root}}^{\infty} \frac{R'(\delta)}{\delta^2}\, d\delta \quad (5)$$

Once a material reaches a critical crack opening displacement, $\delta_c$, the $R$ curve will reach steady state toughness, which implies $R'(\delta) = 0$ for $\delta > \delta_c$. Using this result, the upper limit in Eq. (5) can be replaced by $\delta_c$. This method requires direct energy tracking to measure the amount energy released during crack propagation (actual $R$ curve) along with measurement of notch root opening displacement.

The goal of this work was to use information on cohesive laws to characterize the ability of different adhesives to pro-

duce moisture resistant laminated veneer lumber (LVL) from made from Douglas-fir (*Pseudotsuga menziesii*) veneers and various adhesives. In previous work, we measured $R$ as a function of crack length and then used changes in $R$ caused by exposure of the specimens to moisture cycling [19, 20] to evaluate the adhesives. The hypothesis here is that using the third option to find cohesive laws for each adhesive type and as a function of exposure time will add new information about the durability of those materials. The new results here were to covert previously measure $R(a)$ ($R$ as a function of crack length) to new data for $R(\delta)$ or $R$ as a function of crack opening displacement at the notch root. We then used the resulting $R'(\delta)$ to find cohesive laws using Eq. (5) and this new approach was compared to one prior method. The experimentally measured cohesive laws were fit to a trilinear traction law form (see Fig. 1C) in an attempt to reduce the curves to fewer material properties. The resulting trilinear law properties were examined to add insights into degradation due to moisture exposure and to rank adhesives for durability. The trilinear fits also provided a convenient and realistic traction law for use in numerical modeling to predict the crack propagation properties of LVL. Finally, an analytical model for fiber bridging up to the peak cohesive stress was derived and used to further interpret traction law parameters.

## 2. Materials and Methods

### *2.1. Wood Composite Materials*

LVL billets were manufactured in the laboratory under controlled conditions using all B grade Douglas-fir veneers. Each LVL billet had dimensions 61 × 91 cm (2 × 3 ft), consisted of 11 plies (each 3 mm thick), and used one of the following four adhesives: Wonderbond® EL-35 Emulsion Polymer Isocyanate (EPI), GP® 421G83 RESI-MIX® Phenol Formaldehyde (PF), CASCOPHEN® LT-5210J/CASCOSET® FM-6210 adhesive system Phenol Resorcinol Formaldehyde (PRF), and a one-component Polyvinyl Acetate (PVA). For comparison, experiments were also done on solid Douglas-fir specimens. Detailed descriptions can be found in Refs. [19, 20].

Accelerated moisture exposure of LVL and solid wood was carried out according to ASTM standards [21], but we excluded the steam exposure step. Fracture experiments were done after selected number of cycles each of which consisted of vacuum, pressure, soaking, and drying and denoted here as VPSD cycles. All mechanical tests were done on specimens after drying and after re-equilibrating in a conditioning room (maintained at 21° C and 65% RH) to standard moisture conditions (about 12% moisture content). Details on the VPSD cycles for aging are given elsewhere [19, 20].

### *2.2. Fracture Experiments*

The fracture experiments used double cantilever beam (DCB) specimens in opening mode under displacement control at 2 mm/min. Dimensions of all DCB specimens were $35 \pm 2 \times 35 \pm 2 \times 300 \pm 5$ mm$^3$ and the initial, sawn pre-crack was 100 mm. The crack plane at the edge of each specimen was widened and loading was applied using angle irons inserted into the gap. The long direction of the DCB specimen was the wood grain or longitudinal direction of the wood. The crack plane may be cut either parallel to adhesive bond planes in the LVL or cut to cross all adhesive bond lines. The former is known as an RL fracture (because the normal to the crack plane is in the thickness direction of the veneer, which is the radial direction of solid wood for rotary peeled veneer), while the later is called TL fracture (because normal to the crack plane is in the tangential direction of the wood in the veneers). The L in each fracture mode is for crack growth in the longitudinal direction. Because TL cracks break all bond lines, it has been observed that the adhesive plays a much greater roll in TL fracture than in RL fracture [19]. Because of this greater role of adhesive, all crack propagation experiments reported here for LVL were in the TL direction. For comparison, the solid wood specimens were also studied using TL fracture. In solid wood, a TL crack plane spans multiple growth rings in the specimen.

The load and displacement data during fracture tests were recorded using an Instron 5582 universal testing machine. Crack growth data were collected using the 3D Digital Image Correlation (DIC) technique [22]. For DIC data acquisition, two 50 mm Pentax® lenses (stereo system), attached to high speed Correlated Solutions® cameras mounted on a tripod, were used to capture images during the tests. Images were acquired at 1 Hz. DIC is a technique to map strains by tracking a small subset of pixels in deformed images. To facilitate the DIC analysis, a speckle pattern was applied by painting the surface black and then spraying a random pattern of white dots. VIC 3D® software analyzed the acquired images and calculated strains. The tensile strain normal to the crack plane ahead of the crack tip was monitored throughout the loading. This strain was high near the crack tip and decreased as a function of distance away from the crack tip. Figure 2 shows sample strain profiles for a solid wood specimen. Crack propagation was measured by observing shifts in the position to reach 1% vertical strains between subsequent images. All DIC strain-position data were exported to data sheets for further processing. A Matlab script was written to populate crack propagation data from DIC output based on the 1% strain criterion. [20].

The fracture experiments consisted of multiple replicates each for control (0 VPSD cycles) and after 8, 16, and 24 VPSD cycles. The number of specimens used per treatment were $4 \pm 1$ for solid wood, $8 \pm 2$ for PVA, and $6 \pm 2$ for all other adhesives. Each experiment measured load and crack length as a function displacement. These data were reduced for direct energy calculation of $R$ curves as a function of crack length by methods described elsewhere [8, 12, 19]. An important detail is that these experiments directly measured energy released without any need to impose assumptions about beam or process zone mechanics. The results for all replicates were averaged to get average $R$ curves.

For evaluation of cohesive laws, it is necessary to determine $R$ as a function of $\delta_{root}$ instead of the more commonly measured $R$ as a function of crack growth. To measure $\delta_{root}$,

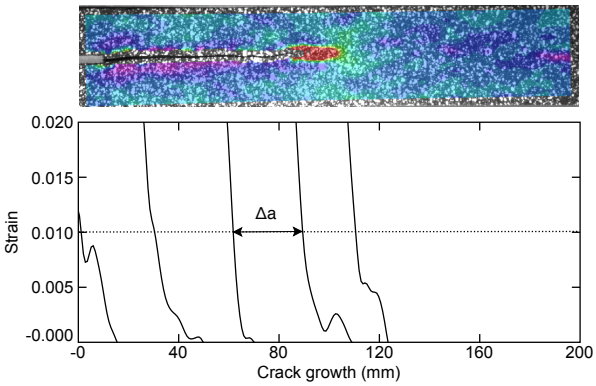


Figure 2: DIC analysis of a solid wood DCB specimen to monitor crack propagation and determine $\delta_{root}$. The colors in the specimen image indicate strain normal to the crack (with red as maximum strain at the crack tip). The plot shows that strain and several time stages along a line though the crack plane. As the crack propagates the strain plot shifts. The shifts between curves (*e.g.*, shift of position to reach 1% strain) indicate the amount of crack growth between the times corresponding to the two curves. Accumulating such crack growths allows accurate tracking of crack growth and was more accurate that attempting visual tracking of crack growth.

the same DIC data used to measure crack length were used to place a virtual extensometer at the notch root of the specimen. In brief, two locations above and below the initial notch root were selected and the net displacement difference between these locations was determined to find $\delta_{root}$. This method is identical to the method used by Lindhagen and Berglund [2] except that it used DIC data and VIC software to measure $\delta_{root}$ rather than a physical crack opening displacement gage. These results were used to convert $R(a)$ curves to $R(\delta_{root})$ curves. Formally, $R(\delta_{root})$ found by this method is only valid up to $\delta_c$ because after reaching $\delta_c$, the process zone edge moves and measuring zone $\delta_{root}$ would require moving the DIC detection locations along with the process zone. Instead, our experiments always measured $\delta$ at the *initial* notch root. After reaching $\delta_c$, however, the material enters steady state propagation with constant toughness $G_{ss}$. In other words, a true $R(\delta_{root})$ curve would increase until $\delta_c$ and then remain at a fixed point with $R(\delta_c) = G_{ss}$ and $\delta_{root}$ constant and equal to $\delta_c$. Our experimental $R(\delta_{root})$ curves are identical to true curves up to $\delta_c$ but then $R(\delta_{root})$ remains constant at $G_{ss}$ while $\delta$ at the original notch root location gets larger than $\delta_c$. Fortunately, determination of cohesive law from $R(\delta_{root})$ only requires information up to the onset of steady state crack growth or up to $\delta_{root} = \delta_c$.

### 2.3. Experimental Determination of Cohesive Laws

We determined cohesive laws for fiber bridging in LVL wood composites and in solid wood from the directly measure $R(\delta_{root})$ curves described above by using Eq. (5). This approach was proposed by Nairn [12], but has not previously been used on real experiments. The first step is to locate the steady state regime, which then determines $\delta_c$. Given $R(\delta_{root})$ up to $\delta_c$, the cohesive laws were then found with a Matlab script using the following algorithm:

1. Divide up experimental data from $\delta_{root} = 0$ to $\delta_{root} = \delta_c$ into $n$ intervals such that $\delta_i = i\delta_c/n$.
2. For each $\delta_i$, pick a smoothing interval size, $k$, and do a linear fit to all data from $R(\delta_{i-k})$ to $R(\delta_{i+k})$ and assign the slope of that fit to be $R'(\delta_i)$ denoted here as $S_i$.
3. The cohesive law is then calculated by taking $\sigma(0) = 0$ and:

$$\sigma(\delta_i) = 2\left[S_i - \frac{\delta_i}{\delta_c}\left(S_n - n\sum_{k=i}^{n-1}(S_{k+1} - S_k)\ln\frac{k+1}{k}\right)\right] \quad (6)$$

This practical equation assumes that $R'(\delta_{root})$ is a piecewise linear function connecting the $S_i$ values and then numerically integrates Eq. (5) using the $n$ experimental data points.

For example, consider a linear softening law of $\sigma(\delta) = \sigma_c(1 - \delta/\delta_c)$. By Eq. (4) the resulting $R(\delta_{root})$ increases linearly from $J_{tip,c}$ up to $G_{ss}$ at $\delta_c$ with slope of $\sigma_c/2$. In other words, $S_i = \sigma_c/2$ for $i$ from 1 to $n-1$ and $S_n = 0$. By Eq. (6), the cohesive law is:

$$\sigma(\delta_i) = \sigma_c\left(1 - \frac{\delta_i}{\delta_c}n\ln\frac{n}{n-1}\right) \quad (7)$$

For a large number of data points ($n \to \infty$), this equation reduces exactly to the linear softening law.

### 2.4. Numerical Modeling

The numerical simulations used the material point method (MPM) and the open-source software NairnMPM [23]. MPM implements explicit cracks by defining a series of massless particles that define the crack path and uses that crack path to partition the analysis into velocity fields above and below the crack plane [24, 25]. MPM can implement traction laws on the crack surfaces by assigning a traction law to one or more crack particles along the crack [12]. One use of such traction laws is to simulate crack propagation and process zone development in fiber-bridging materials [7, 8, 12].

Simulations that include both crack tip growth and formation of a cohesive zone require a method that can dynamically create cohesive zones. In brief, the simulation starts with an initial crack and no cohesive zone (this approach differs from the common finite element analysis (FEA) method of pre-inserting cohesive elements at the start of the calculations). When the crack tip energy release rate exceeds, $J_{tip,c}$, the crack tip propagates and a cohesive zone is inserted in its wake. As the simulation proceeds, the crack tip continues to propagate at $J_{tip,c}$ and the cohesive zone grows and develops. Eventually, $\delta_{root}$ reaches $\delta_c$ causing the cohesive zone to start failing and the propagation reaches steady state crack growth. The simulated $R$ curve is determined using Eq. (4). MPM can handle this dynamic cohesive zone analysis as explained elsewhere [7, 8, 12].

One challenge in simulating crack propagation is dealing with kinetic energy. In all numerical models of crack propagation, crack growth is simulated by enlarging a crack, which

can be by separating nodes in FEA or adding a new crack tip particle in MPM. This change will cause a release of energy. In computational mechanics codes that correctly conserve energy, the energy released by changing crack length will convert mostly to kinetic energy. As simulations proceed, the kinetic energy can dominate the results or cause instabilities. Now, in real materials, the energy released is mostly absorbed by the material in processes required to create the new crack surfaces. One way to model real absorbed energy is by adding damping to the numerical model, but it is extremely difficult to add realistic damping. A recent paper on crack propagation in MPM calculations has proposed a new form of damping called PIC damping [26]. It selectively damps out kinetic energy in regions of rapid variations in velocity. It appears to work well for crack propagation by damping out kinetic energy without over damping to cause unrealistic results. All simulations here used the PIC damping method proposed in Ref. [26].

## 3. Results and Discussion

### *3.1. Experimental $R(\delta)$ Curves*

Figure 3A shows $R(a)$ curves for PVA LVL as a function of number of VPSD crack cycles as a function of crack growth (note that this crack growth was determined from propagation of the crack tip and not the notch root). For calculations of cohesive laws, we replotted $R(\delta)$ curve as a function of crack opening displacement at the notch root (see Fig. 3B). $R$ curves as a function of crack length, $a$, and converted to be a function crack tip opening displacement, $\delta$, for PVA LVL as a function of number of VPSD cycles are shown in Fig. 3. Both $R(a)$ and $R(\delta)$ clearly show degradation as the number of VPSD cycles increased. The generic shapes are similar. Both curves initiate at the same toughness and then increase due to fiber bridging. At long crack length, the curves tend to plateau at a steady state toughness. Note that the curvatures or rate of approaching steady state differ for $R(a)$ and $R(\delta)$. The determination of $\sigma(\delta)$ uses the slope of the $R$ curve and requires those slopes to be found from $R(\delta)$ curves. Also note that plateau values differ slightly between $R(\delta)$ and $R(a)$. All data were initially recorded as a function of time as the reference parameter for cross plotting. Because the averaging process may include different ranges of $a$ or $\delta$, the average $R$ values showed some minor differences as well.

The algorithm for finding cohesive law depends on experimental $\delta_c$. In theory, $\delta_c$ is the point where $R(\delta)$ becomes flat and equal to $G_{ss}$, but in heterogeneous materials, including wood based materials, the determination of $\delta_c$ can be challenging. We approximated $\delta_c$ for PVA LVL as 6 mm and for other materials as 3.5 mm. It is important to note that solid wood does not actually reach $G_{ss}$, but we assumed it is close to 3.5 mm to have a reference point for determining its bridging traction.

### *3.2. Experimental $\sigma(\delta)$ Curves*

Fiber bridging cohesive laws ($\sigma(\delta)$), determined as explained in Materials and Methods, for PVA LVL as a function

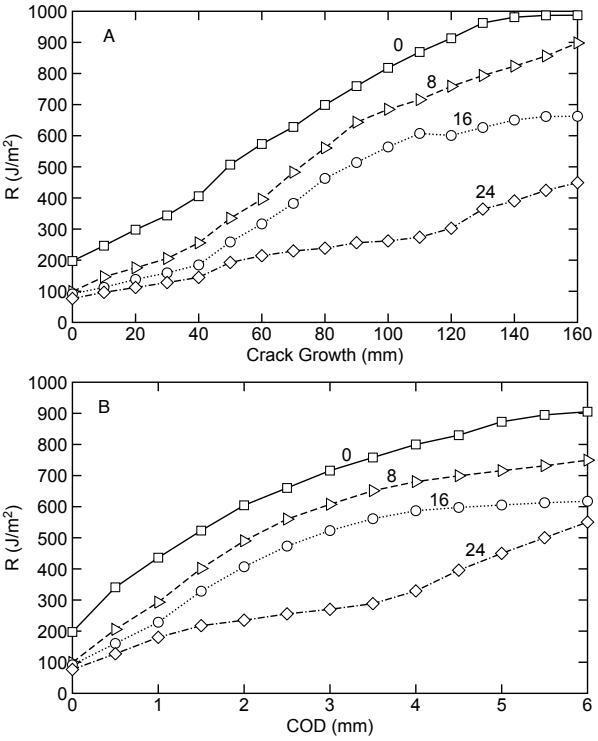


Figure 3: $R$ curves of PVA LVL as a function of the number of VPSD cycles: A. $R$ as a function of crack length. B. $R$ as a function of the crack opening displacement, $\delta$.

of number of VPSD cycles are given in Fig. 4A. The bridging stress profiles are characterized by an initial sharp increase up to critical cohesive stress ($\sigma_c$) and then monotonic decrease down to zero stress at critical $\delta_c$. While a similar shape has been reported for bridging ceramics [27], prior valid cohesive laws for fiber reinforced polymer composites did not report an initial rise [2]. The cohesive stress for PVA LVL is well correlated with aging and decreased as the number of VPSD cycles increased. The post-peak, or softening region, of the cohesive laws were less affected by aging. Figure 5 gives bridging stress profiles for all other adhesives and for solid wood as a function of VSPD cycles. All $\sigma(\delta)$ had similar generic shapes, but unlike $\sigma(\delta)$ for PVA-LVL, the effects of VPSD cycles on other materials were less apparent. Vasic and Smith [17, 18] previously determined a cohesive law in spruce, but their results were very different. Their peak cohesive stress was 0.597 MPa and critical crack opening displacement was 32 $\mu$m. The differences could be due to species (unlikely) or to specimen size. Their expeirments were limited to very small specimens and small amounts of crack growth (for work in a scanning electron microscope). With more crack growth, we see much higher cohesive stress up to much higher crack opening displacement. Both approaches show softening behavior.

Figure 6 compares bridging tractions of solid wood and LVLs made with various adhesives for control specimens or for 0 VPSD cycles. Comparing the different LVL specimens, PVA and PRF had the largest and smallest bridging stresses,

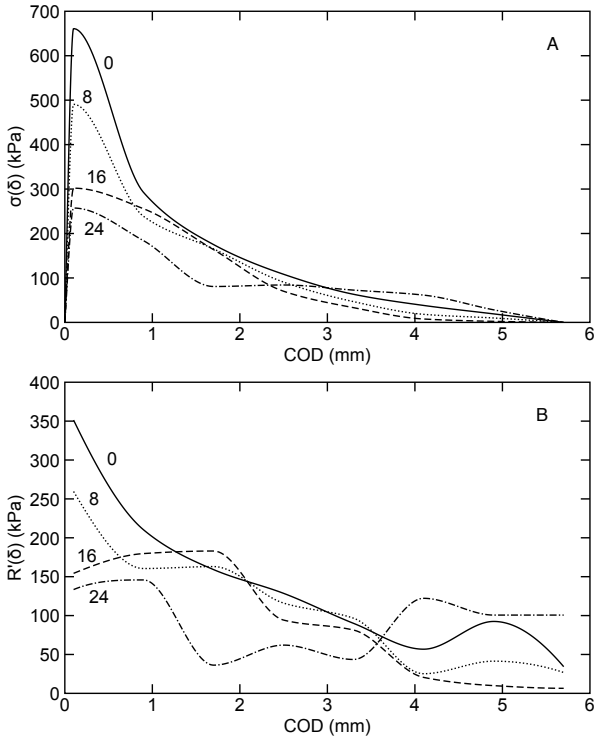


Figure 4: $\sigma(\delta)$ curves of PVA LVL as a function of the number of VPSD cycles: A. $\sigma(\delta)$ found using Eq. (5). B. $\sigma(\delta)$ found using $R'(\delta)$.

respectively. Comparing LVL to solid wood, the cohesive stress due to bridging fibers in solid wood (filled black curve) is far below the cohesive stresses for all LVL specimens. This observation implies that fiber bridging is not simply stress carried by wood fibers bridging the crack, but is rather a more complex interaction between wood and adhesive. The adhesive either reinforces the bridging fibers, making them stronger, or allows a greater number of bridging fibers. Images for fracture surfaces in solid wood and PVA LVL are given in Fig. 7. While the fracture surfaces of solid wood were relatively smooth, LVL fracture surfaces exhibited many broken fibers and fiber bundles. These pictures emphasize the role of fiber bridging in enhancing LVL toughness and are consistent with the considerable difference of bridging tractions between solid wood and LVL seen in Fig 6.

The cohesive laws measured here used a new method inherent in Eq. (5). Because most prior work has simply equated $\sigma(\delta)$ to $R'(\delta)$, two questions that arise are — how to evaluate prior methods and how to judge their accuracy? The first step in evaluating prior work is to assess how they measured $R$ during process zone development. Did they directly track energy or did they use simple fracture equations based on end load (or displacement) and crack length (*e.g.*, beam theory on DCB specimens where the beam theory cannot account for fiber bridging before the bridging law is known [11])? Only direct methods can give actual $R$ curves. The methods used here are acceptable. Another acceptable approach could be to use an experimental compliance calibration method [1]. Basic linear elastic fracture mechanics

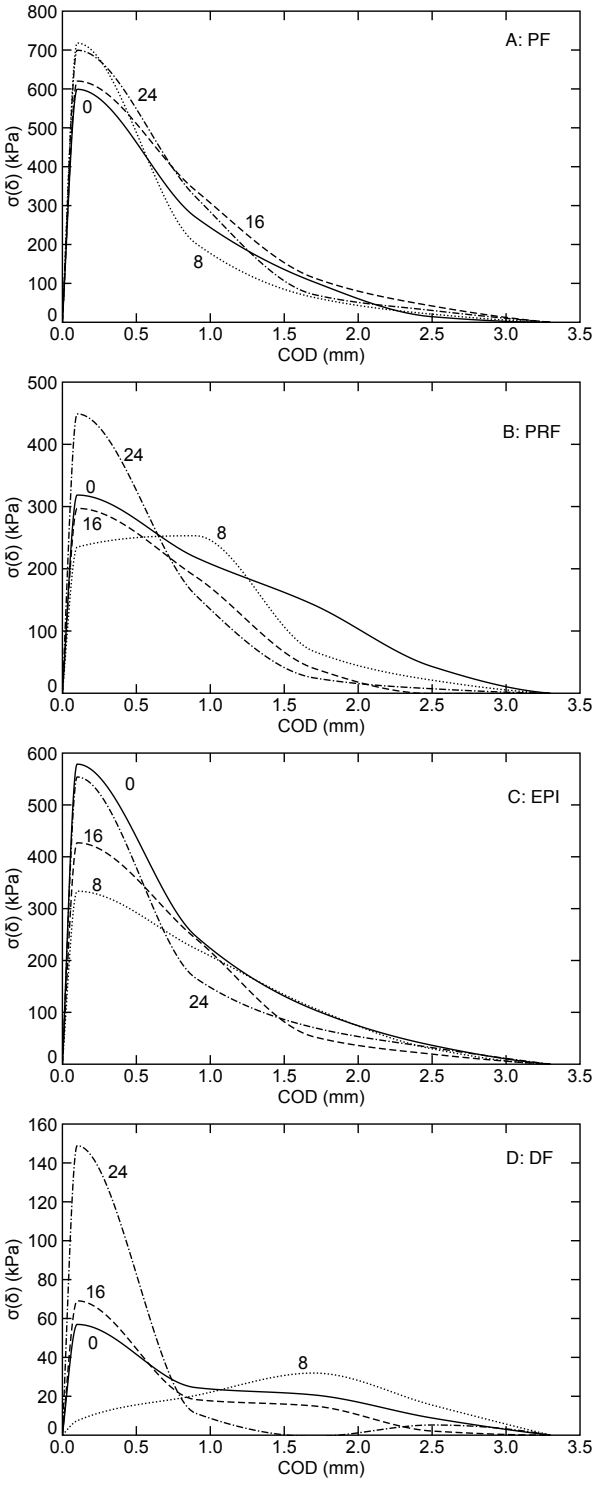


Figure 5: $\sigma(\delta)$ curves as a function of the number of VPSD cycles calculated using Eq. (5): A. PF LVL. B. PRF LVL. C. EPI LVL. D. Solid wood Douglas-fir.

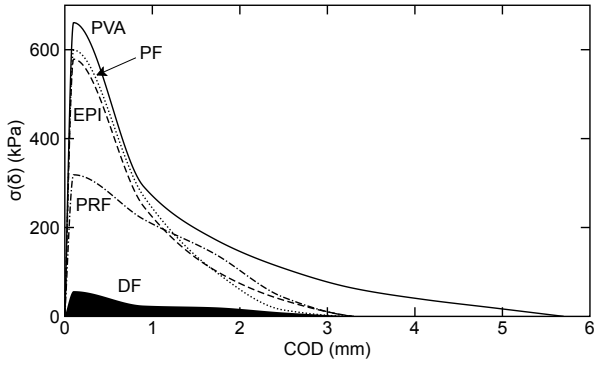


Figure 6: $\sigma(\delta)$ curves of all LVL types compared to solid wood Douglas-fir for control specimens (or 0 VPSD cycles).

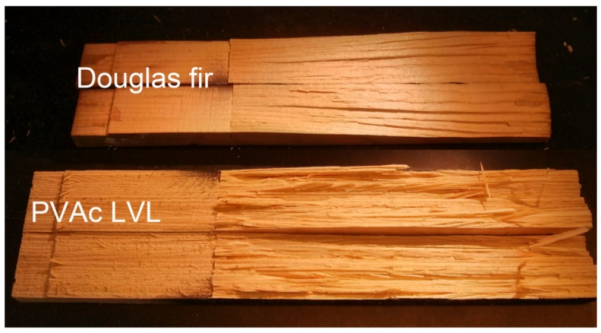


Figure 7: Fracture surfaces for DCB specimens of solid Douglas-fir wood (top) and PVA LVL (bottom) [19].

equations (*e.g.*, $R = P^2a^2/(BEI)$ for DCB where $P$ is load, $a$ is crack length, $B$ is thickness, $E$ is modulus, and $I$ is moment of inertia) are never correct. For the special case of pure moment loading, such equations do give $J_{ff}(\delta_{root})$, but that is not $R$ during process zone specimen. For the more common end-loaded specimens, the simple equations give neither $R$ nor $J_{ff}(\delta_{root})$. The next evaluation step is to see how the $R$ results were converted to $\sigma(\delta)$. For those who measured the actual $R$ curve, the cohesive law must be determined from Eq. (5) (assuming their process zones could be approximated by an elastic damage mechanism). The prevalent use of $\sigma(\delta) = R'(\delta_{root})$ is, at best, inaccurate, and, potentially, a serious error. For those who correctly used beam theory to determine $J_{ff}(\delta_{root})$ (which only applies to pure moment loading), the cohesive law can be derived from simple derivative in Eq. (3). For those who measured neither $R$ nor $J_{ff}(\delta_{root})$, no method can extract a valid cohesive law.

Lastly, what is the consequence of finding $\sigma(\delta)$ from $R'(\delta)$, which the above fracture mechanics analysis of a cohesive zone suggests is not correct and should be replaced by Eq. (5). Fig. 4B shows $\sigma(\delta)$ from $R'(\delta)$ using the same $R(\delta)$ that was used to find $\sigma(\delta)$ from Eq. (5) in Fig. 4A. While general softening behaviors are seen in both methods, the $\sigma(\delta)$ details are different. The new method (Fig. 4A) shows increases up to the cohesive stress, while it was difficult to detect an increasing regime by the $R'(\delta_{root})$ method (Fig. 4B). The peak cohesive stresses by the two methods differ by nearly a factor of 2. The overall softening shapes appear to be more smoothly monotonic in the new method compared to the $R'(\delta_{root})$ method. Finally, the areas under the cohesive should be equal to total bridging toughness defined by $G_B = G_{ss} - J_{tip,c}$. Mathematically, integration of both Eq. (5) and $R'(\delta)$ leads to $G_B$. Using the curves in Fig. 4, on both new and $R'(\delta_{root})$ methods are reasonably close to $G_B$ with average error of 5-10%. In other words, examining the area under a cohesive law is not a good method for judging validity of that law. Sorenson *et al.* [14] similarly compared their FBG method described in the introduction for directly finding $\sigma(\delta)$ to the $R'(\delta)$ method (but we note their measured $R(\delta)$ was found by fracture mechanics equation that gives neither $R$ nor $J_{ff}(\delta_{root})$). Although they claimed both approaches are correct and described the two results as similar, they had differences in cohesive stresses (also a factor of 2). We suggest such differences mean the two methods are different and only $\sigma(\delta)$ from their FBG method should be considered as correct.

### 3.3. Representation as Trilinear Traction Law

Because comparing cohesive law curves (especially when they overlap) is challenging, we next attempted to reduce the fiber bridging properties for different adhesives and different exposure times to a smaller number of parameters by fitting the cohesive laws to a characteristic function. All cohesive laws in Figs. 4 to 6 show non-linear softening. We first fit to exponential softening, but that did not work well. Instead, all results could be reasonably represented by a trilinear traction law (see Fig. 1C). A trilinear traction law, depends on five properties — $(\delta_1, \sigma_1)$ and $(\delta_2, \sigma_2)$ breakpoints and a critical $\delta_c$. The total toughness of the modeled process zone is the area under the traction law curve, which is given by:

$$J_c = \frac{1}{2}(\sigma_1\delta_2 + \sigma_2(\delta_c - \delta_1)) \tag{8}$$

A potential interpretation of a trilinear law is that it is modeling two physical mechanisms. The first failure mechanism can be identified with the area under the first peak and bounded by the dotted line in Fig. 1C. Its toughness is $J_1 = (\sigma_1\delta_2 + \sigma_2\delta_1)/2$ and is likely associated with strong and short bridging fibers close to the crack tip. The second mechanism is the remaining area ($J_2 = \sigma_2\delta_c/2$) and is likely associated with longer and weaker bridging fibers. The reasons for reduction of data to a trilinear traction law were twofold: 1. To reduce to fewer experimental variables that can be examined to give insights about effects of moisture cycling. 2. To provide a convenient form for input of a cohesive law into numerical models (see next section).

Trilinear fits for cohesive laws in control specimens are given in Fig. 8. It was not possible to accurately determine all five trilinear law properties. We decided to fix $\delta_1 = 0.1$ mm and $\delta_2 = 1.0$ mm, use $\delta_c$ from above analysis. Next, a MatLab script was written to find non-linear best fits to experimental $\sigma(\delta)$ by varying the two cohesive stresses, $\sigma_1$ and $\sigma_2$, and the two energies, $J_1$ and $J_2$, subject to the constraint

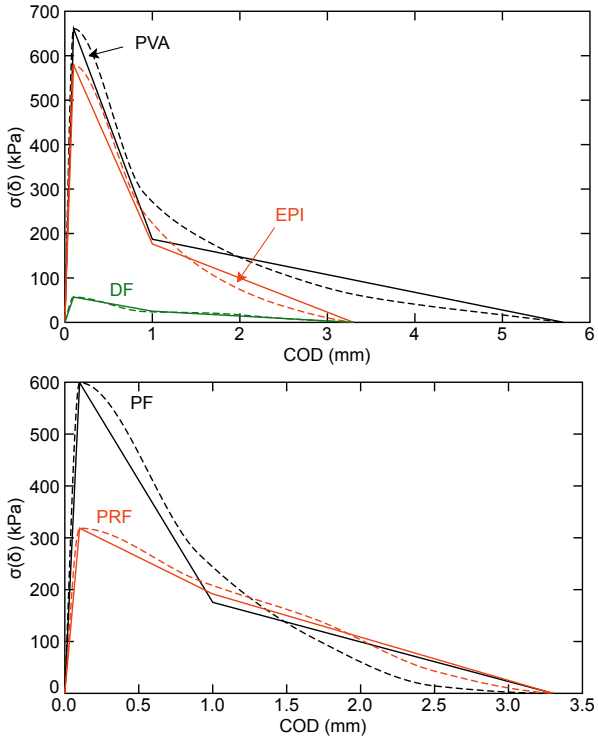


Figure 8: Application of trilinear cohesive law to control PVA, PF, EPI, PRF, and DF. The dashed lines are experimental results and solid lines are the trilinear fits

that $J_1 + J_2$ matched the measured steady-state toughness. The resulting trilinear parameters for all specimen conditions are in Table 1. The last two columns give degradation rate (per cycle) for that property and correlation coefficient for the linear fit. Overall, only a few properties showed degradation and were well correlated. Those properties with correlation coefficient above 0.8 are indicated in bold. For PVA, all properties degraded with cycles. For EPI and PRF, the initial peak is not affected, but the $\sigma_2$ and $J_2$ terms did degrade. Comparing $J_2$ (or $\sigma_2$) degradation rates, PRF degraded faster than EPI. For both PF and DF, the traction laws were uncorrelated with VPSD cycles. These results suggest that PF is the most durable adhesive, followed by EPI, PRF, and PVA, in that order. This ranking is identical to the rankings derived by Mirzaei *et al.* [20] that were done by observations of $R$ curve changes. The fact that PVA was the only material showing correlated degradation of $\sigma_1$ and $J_1$ might be potentially explained by adhesive penetration. PVA penetrated the least of all four adhesives into the wood cells [20]. The penetration of other adhesives may have protected the fibers associated with the first peak while they are left open to degradation in PVA composites. Because VPSD cycles are known to affect DF toughness [19], the lack of correlations for DF indicates that moisture affects the initiation toughness much more than the fiber bridging properties.

### *3.4. Fiber Bridging Model*

To gain physical insight into the cohesive stress, we attempted to derive an expected cohesive law as a function of

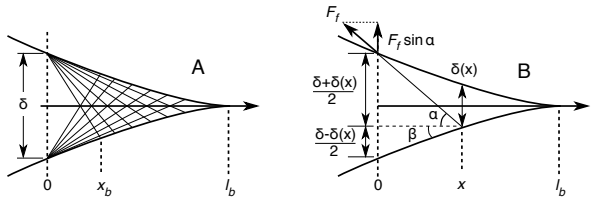


Figure 9: A. Fiber bridging zone shows fibers on both surfaces. B. A single bridged fiber from the notch root (at $x = 0$) to location $x$ on the bottom. $\delta$ is the crack opening displacement at the notch root and $\delta(x)$ is the opening at $x$. $\boldsymbol{F}_f$ is the force on the single fiber and $\alpha$ and $\beta$ indicate two key angles.

the bridging fiber strength, fiber area, and number of bridging fibers. Figure 9A shows a fiber bridging zone with fibers bridging from the zone edge (at $x = 0$) to the opposite surface. The location $x_b$ is the point at which the bridged fiber is no longer peeled from the opposite surface or has elongated to the fiber's breaking strain, which ever gives a larger $x_b$. The force due to bridging fibers at $x = 0$ will be sum of forces from all fibers from $x_b$ to $l_b$ where $l_b$ is current length of the bridging zone. This analysis is restricted to small zones and small openings and is thus aimed at finding cohesive stress only in the initial phase or up to the peak cohesive stress, $\sigma_c$. In this initial phase, it is assumed that the fibers between $x_b$ and $l_b$ have remained intact and have formed at some constant bridging rate (bridged fibers per unit length). Figure 9B focuses on a single fiber starting on the top surface and ending on the bottom surface at position $x$. The fiber strain is approximately:

$$\varepsilon_f = \frac{\sqrt{x^2+(\delta+\delta(x))^2/4}}{\sqrt{x^2+(\delta-\delta(x))^2/4}} - 1 \approx \frac{k^2 r}{2(1-r)^2} \qquad (9)$$

where $\delta$ and $\delta(x)$ are crack opening displacements at the edge of the zone and at $x$, and $r = 1 - x/l_b$. For this small displacement condition, it is assumed crack opening displacement is linear ($\delta(x) = k(l_b - x)$) and that its slope ($k$) is small. Using the small $k$ result of $\sin\alpha = k(1+r)/(2(1-r))$, the total force in the $y$ direction per unit length at $x = 0$ due to all bridging fibers ending at $x$ is

$$F_y(x) = \frac{E_f A_f N_b k^3}{4(l_b - x_b)} \frac{r(1+r)}{(1-r)^3} \qquad (10)$$

where $E_f$ is fiber modulus, $A_f$ is fiber area, and $N_b$ is total number of bridged fibers at $x = 0$ (which are assumed to have the opposite ends spread out uniformly from $x = x_b$ to $l_b$). The total force at $x = 0$ is found by integrating $F_y(x)$ from $x_b$ to $l_b$. Converting to an integral over $r$ and dividing that force by unit area, the cohesive stress is

$$\begin{aligned} \sigma(\delta) &= \frac{E_f A_f \rho_b k^3}{4 r_b} \int_0^{r_b} \frac{r(1+r)}{(1-r)^3}\, dr \\ &= \frac{E_f A_f \rho_b k^3}{4} \left( \frac{2r_b - 1}{(1-r_b)^2} - \frac{\ln(1-r_b)}{r_b} \right) \end{aligned} \qquad (11)$$

where $\rho_b$ is the bridged fiber density (number of bridged fibers per unit area) and $r_b = 1 - x_b/l_b$.

Table 1: Fiber bridging properties for all LVL materials and for solid wood Douglas-fir. The stresses ($\sigma_1$ and $\sigma_2$) are in kPa, the toughnesses ($J_1$ and $J_2$) are in J/m$^2$; the bridging zone lengths at peak stress ($l_b$) are in mm, and the bridging densities ($\rho_b$) are in mm$^{-2}$).

| Matl. | Value | 0 | 8 | 16 | 24 | Slope | $R^2$ |
|---|---|---|---|---|---|---|---|
| PVA | $\sigma_1$ | 661 | 491 | 302 | 257 | **-17.5** | **0.94** |
| | $J_1$ | 321 | 238 | 144 | 123 | **-8.7** | **0.94** |
| | $\sigma_2$ | 187 | 154 | 147 | 141 | **-1.8** | **0.82** |
| | $J_2$ | 533 | 439 | 418 | 403 | **-5.1** | **0.82** |
| | $l_b$ | 6.7 | 5.3 | 6.4 | 6.5 | | |
| | $\rho_b$ | 40-111 | 24-66 | 17-49 | 15-42 | | |
| EPI | $\sigma_1$ | 579 | 334 | 427 | 554 | 0.23 | 0.00 |
| | $J_1$ | 281 | 158 | 206 | 271 | 0.24 | 0.00 |
| | $\sigma_2$ | 177 | 170 | 144 | 117 | **-2.6** | **0.94** |
| | $J_2$ | 291 | 281 | 238 | 193 | **-4.2** | **0.94** |
| | $l_b$ | 8.5 | 6.1 | 6.6 | 8.5 | | |
| | $\rho_b$ | 44-124 | 18-51 | 26-71 | 42-119 | | |
| PRF | $\sigma_1$ | 319 | 235 | 297 | 449 | 5.7 | 0.42 |
| | $J_1$ | 150 | 109 | 143 | 220 | 3.1 | 0.46 |
| | $\sigma_2$ | 192 | 163 | 104 | 81 | **-4.9** | **0.97** |
| | $J_2$ | 316 | 269 | 172 | 133 | **-8.1** | **0.97** |
| | $l_b$ | 5.6 | 4.1 | 6.1 | 7.4 | | |
| | $\rho_b$ | 16-45 | 9-24 | 16-45 | 30-84 | | |
| PF | $\sigma_1$ | 599 | 718 | 620 | 700 | 2.5 | 0.20 |
| | $J_1$ | 291 | 353 | 299 | 340 | 1.2 | 0.15 |
| | $\sigma_2$ | 176 | 122 | 228 | 190 | 1.9 | 0.19 |
| | $J_2$ | 290 | 201 | 377 | 314 | 3.1 | 0.19 |
| | $l_b$ | 4.6 | 6.6 | 6.0 | 6.7 | | |
| | $\rho_b$ | 25-70 | 42-119 | 34-94 | 42-118 | | |
| DF | $\sigma_1$ | 57 | 7 | 69 | 149 | 4.2 | 0.55 |
| | $J_1$ | 27 | 2 | 347 | 74 | 2.2 | 0.55 |
| | $\sigma_2$ | 25 | 34 | 166 | 3 | -1.0 | 0.68 |
| | $J_2$ | 42 | 56 | 26 | 5 | -1.7 | 0.68 |
| | $l_b$ | 4.4 | 5.2 | 5.8 | 6.3 | | |
| | $\rho_b$ | 2-6 | 0.3-1 | 4-10 | 8-24 | | |

If $x_b$ is determined by breaking strain of the fiber, it is found by solving for $r$ at which $\varepsilon_f = \varepsilon_{f,b}$:

$$r_b = 1 + \phi^2 - \phi\sqrt{2+\phi^2} \qquad \text{where} \qquad \phi = \frac{k}{2\sqrt{\varepsilon_{f,b}}} \quad (12)$$

Substituting $r_b$ into Eq. (11) and expanding as a series in $k$, and using $k = \delta/l_b$ leads eventually to:

$$\sigma(\delta) = \frac{A_f \rho_b}{2l_b}\sigma_{fb}\delta + \mathrm{O}[k^2] \quad (13)$$

where $\sigma_{f,b} = E_f \varepsilon_{f,b}$ is the bridging fiber strength. If peeling controls $x_b$, then solve for $r$ such that the individual fiber force leads to energy release rate for peeling [28] that equals the peeling toughness, $G_c$, for the fiber

$$G_c = \frac{F_f}{W_f}\big(1-\cos(\alpha+\beta)\big) = \frac{A_f E_f}{4W_f}\frac{k^4 r}{(1-r)^4} \quad (14)$$

where $W_f$ is width of the peeling surface. Although solving this $4^{th}$ order polynomial equation and expanding as a series in $k$ is difficult by hand, it can be done easily in Mathematica [29] with the result:

$$\sigma(\delta) = \frac{A_f \rho_b}{2l_b}\sqrt{\frac{E_f G_c}{r_f}}\delta + \mathrm{O}[k^2] \quad (15)$$

where fibers have been approximated as cylindrical ($A_f = \pi r_f^2$ and $W_f = \pi r_f$). It is tempting to extend this approach beyond the peak stress, but at higher $\delta$, it is likely that some bridging fibers become damaged or broken (causing $E_f$, $N_b$, and maybe more terms to no longer be constant), and that opening becomes large (causing $k$ to be too large and $\delta$ to be nonlinear). We claim this type of analysis is only appropriate during linear rise up to the maximum cohesive stress.

In principle, given properties of the bridging fibers, we can calculate the bridging density, $\rho_b$. Although many bridging fiber properties are not known, we can propose a rational range of properties. First, we looked at the amount of crack growth required to reach the peak cohesive stress, which is equal to $l_b$. The results for all materials in Table 1 ranged from 4 to 8 mm. This range is close to the range for individual

wood fibers, known as tracheid cells, typically found in softwood Douglas-fir (1.7-7 mm) [30], suggesting that bridged fibers leading to peak cohesive stress may be similar to tracheid fibers. The properties for individual tracheid fibers can be estimated as $\sigma_f = 648$ MPa , $E_f = 40$ GPa [31], and $r_f = 20$ $\mu$m [30]. On the other hand, the bridged fibers may be multiple tracheid fibers bound together (naturally of by the adhesive) and have properties closer to solid wood, such as $\sigma_f = 100$ MPa, $E_f = 10$ GPa [32], and $r_f = 200$ $\mu$m (*i.e.*, 10 tracheid fibers in the radius of the bundle). The peel out toughness likely ranges from close to initiation toughness for Douglas-fir (200 J/m$^2$) to some lower value (*e.g.*, 50 J/m$^2$). Substituting these values into Eqs. (13) and (15) with $\delta = 0.1$ mm for all materials gives a range in bridged fiber density from 10 to 120 mm$^{-2}$ for LVL and from 0.3 to 24 mm$^{-2}$ for solid Douglas-fir (all ranges are in Table 1). In all calculations, the peeling mechanics determined the cohesive stress, but the differences between peeling and fiber breaking were small.

### 3.5. *Validation — Numerical Modeling*

The previous sections presented a new approach to experimental determination of the cohesive law for fiber bridging in composites and reduction of those laws to a form suitable for use in modeling (a trilinear traction law). One use for such laws is to insert them into numerical models to predict fracture properties in the presence of fiber bridging. To validate our experimental curves, we used them in an MPM model for crack growth in which propagation of the crack tip at a crack tip toughness ($J_{tip,c}$) leaves a cohesive zone in its wake. The notch root of the bridging zone debonds when the crack opening displacement reaches the critical value for the bridging law. During process zone development, the crack tip propagates while the notch root remains fixed. Once crack growth reaches steady state, the crack tip and notch root propagate in parallel. The validation goal was to determine if simulated $R$ curves as a function of crack length derived using the experimentally determined $\sigma(\delta)$ laws will reproduce the experimentally determined $R(a)$ results.

The details on the MPM simulation of crack growth are given in the materials and methods section. We input the trilinear cohesive law properties in Table 1 for each LVL product, used actual specimen geometry and loading conditions, and numerically propagated the crack tip and bridging zone up to steady state conditions. Comparisons of simulated $R$ curves (solid lines) to experimental results for control specimens of each (with the error bars) are given in Fig. 10. The experimental results are from Ref. [20]. In general, the simulations do a good job of matching experimental results, thus demonstrating self-consistency of experiments, the method to find $\sigma(\delta)$, and the numerical model for $R$ curves. The simulated curves do not match all details of the experiments because the use of trilinear fits, as opposed to more complex laws, will numerically smooth over those details.

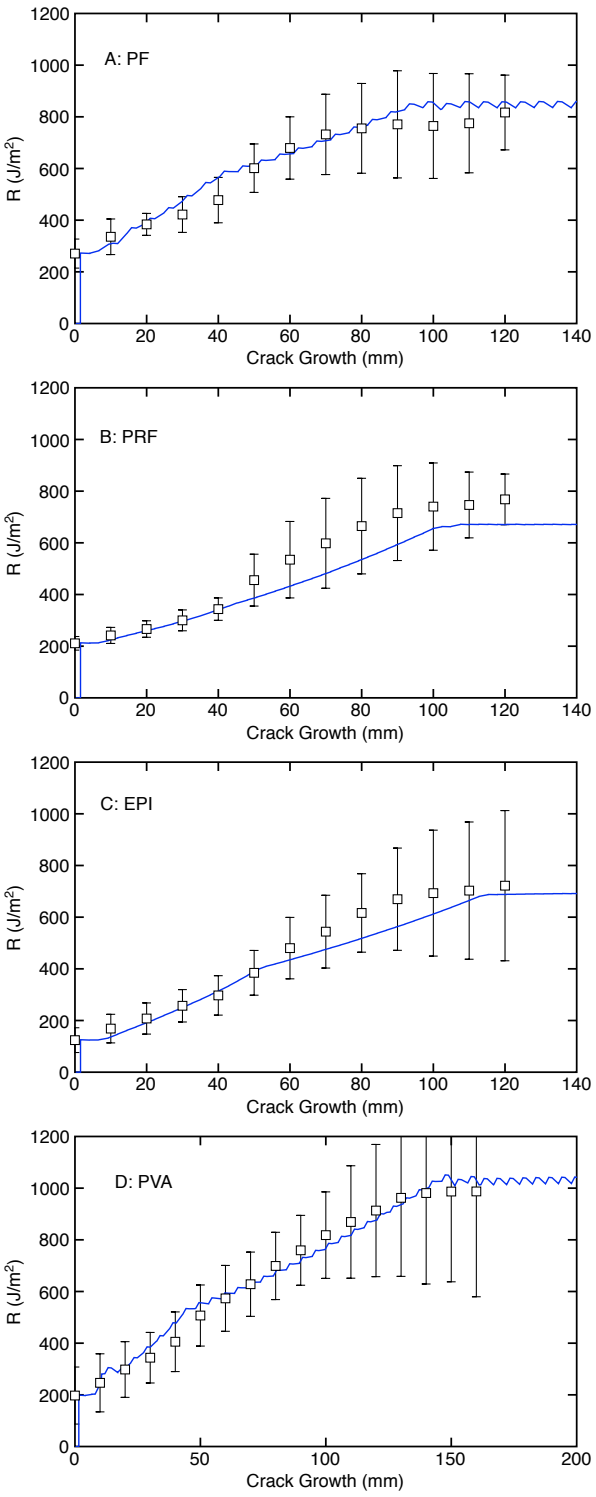


Figure 10: Experimental $R(a)$ curves of all control LVL materials (symbols with error bars) compared to simulated $R$ curves using MPM modeling. A. PF LVL. B. EPI LVL. C. PRF LVL. D. PVA LVL.

## 4. Conclusions

We explained why many prior methods that determined cohesive laws from $R'(\delta)$ need to be rethought; in most cases, the specimens that were used are not suitable for simple differentiation of $R(\delta)$. We replaced that prior method with the new method in Eq. (5). In brief, the experiments must directly measure energy released to calculate an actual $R(\delta)$ curve and then find cohesive law from Eq. (5). The new approach was used to determine cohesive laws for a series of Douglas-fir LVL specimen with different adhesives and after exposure to moisture exposure cycles. Examination of the cohesive laws was used to rank adhesives for their ability to provide durable LVL products and that ranking agreed with a prior ranking determined by other methods [20]. Finally, analytical and numeral modeling methods were used to gain insights into fiber bridging mechanics and to demonstrate an MPM numerical model that can propagate cracks, develop fiber bridging zones, and reach steady state propagation. The MPM numerical modeling results agreed with experimental $R(a)$ curves.

## Acknowledgments

Financial support was provided by the National Science Foundation Industry/University Cooperative Research Center for Wood-Based Composites, Award No. IIP-1034975. We thank Momentive® Specialty Chemicals and Georgia Pacific Chemicals® for supplying all adhesives and veneer materials.

## References

[1] S. Hashemi, A. J. Kinloch, J. G. Williams, The analysis of interlaminar fracture in uniaxial fibre reinforced polymer composites, Proc. R. Soc. Lond. A427 (1990) 173–199.
[2] J. E. Lindhagen, L. A. Berglund, Application of bridging-law concepts to short-fibre composites part 1: DCB test procedures for bridging law and fracture energy, Comp. Sci. & Tech 60 (2000) 871–883.
[3] R. Nalla, J. Kruzic, R. Ritchie, On the origin of the toughness of mineralized tissue: microcracking or crack bridging?, Bone (2004) 790–798.
[4] I. Smith, E. Landis, E. Gong, Fracture and Fatigue in Wood, John Wiley & Sons, Ltd., 2003.
[5] M. Shir Mohammadi, J. A. Nairn, Crack propagation and fracture toughness of solid balsa used for cores of sandwich composites, Journal of Sandwich Structures and Materials 16 (1) (2014) 22–41.
[6] E. Wilson, M. S. Mohammadi, J. A. Nairn, Crack propagation fracture toughness of several wood species, Advances in Civil Engineering Materials 2 (1) (2013) 316–327.
[7] N. Matsumoto, J. A. Nairn, Fracture toughness of wood and wood composites during crack propagation, Wood and Fiber Science 44 (2) (2012) 121–133.
[8] N. Matsumoto, J. A. Nairn, The fracture toughness of medium density fiberboard (MDF) including the effects of fiber bridging and crack-plane interference, Eng. Fract. Mech. 78 (2009) 2748–2757.
[9] A. Sinha, J. A. Nairn, R. Gupta, The effect of elevated temperature exposure on the fracture toughness of solid wood and structural wood composites, Wood Science & Technology 44 (2012) 1127–1149.
[10] G. Bao, Z. Suo, Remarks on crack-bridging concepts, Appl. Mech. Rev. 45 (6) (1992) 355–366.
[11] J. R. Rice, A path independent integral and the approximate analysis of strain concentration by notches and cracks, J. Applied Mech. June (1968) 379–386.
[12] J. A. Nairn, Analytical and numerical modeling of R curves for cracks with bridging zones, Int. J. Fract. 155 (2009) 167–181.
[13] B. D. Manshadi, A. P. Vassilopoulos, J. Botsis, A combined experimental/numerical study of the scaling effects on mode i delamination of {GFRP}, Composites Science and Technology 83 (2013) 32 – 39.
[14] L. Sorensen, J. Botsis, T. Gmur, L. Humbert, Bridging tractions in mode I delamination: Measurements and simulations, Composites Sciences and Technology 68 (2008) 2350–2358.
[15] S. Stutz, J. Cugnoni, J. Botsis, Crack – fiber sensor interaction and characterization of the bridging tractions in mode i delamination, Engineering Fracture Mechanics 78 (6) (2011) 890 – 900.
[16] S. Stutz, J. Cugnoni, J. Botsis, Studies of mode i delamination in monotonic and fatigue loading using FBG wavelength multiplexing and numerical analysis, Composites Science and Technology 71 (4) (2011) 443 – 449.
[17] S. Vasic, I. Smith, Bridging crack model for fracture of spruce, Engineering Fracture Mechanics 69 (6) (2002) 745–760.
[18] S. Vasic, Applications of fracture mechanics to wood, Ph.D. thesis, University of New Brunswick (Canada) (2000).
[19] B. Mirzaei, A. Sinha, J. A. Nairn, Using crack propagation fracture toughness to characterize the durability of wood and wood composites, Materials & Design 87 (2015) 586–592.
[20] B. Mirzaei, A. Sinha, J. A. Nairn, Assessing the role of adhesives in durability of laminated veneer lumber (lvl) by fracture mechanics, Holzforschung (2016). doi:http://dx.doi.org/10.1515/hf-2016-0193.
[21] ASTM Standard D2559, Standard specification for adhesives for bonded structural wood products for use under exterior exposure conditions., ASTM International, West Conshohocken, PA (2012).
[22] M. A. Sutton, W. J. Wolters, W. H. Peters, W. F. Rawson, S. R. McNeil, Determination of displacement using improved digital image correlation method, Image and Vision Computing 1 (3) (1983) 133–139.
[23] J. A. Nairn, Material point method (NairnMPM) and finite element analysis (NairnFEA) open-source software, http://osupdocs.forestry.oregonstate.edu/index.php/Main_Page (2015).
[24] J. A. Nairn, Material point method calculations with explicit cracks, Computer Modeling in Engineering & Sciences 4 (2003) 649–664.
[25] Y. Guo, J. A. Nairn, Calculation of j-integral and stress intensity factors using the material point method, Computer Modeling in Engineering & Sciences 6 (2004) 295–308.
[26] J. A. Nairn, Numerical simulation of orthogonal cutting using the material point method, Engineering Fracture Mechanics 149 (2015) 262–275. doi:http://dx.doi.org/10.1016/j.engfracmech.2015.07.014.
[27] S. Gallops, Development and validation of a fatigue reliability method for bridging materials, Ph.D. thesis, Oregon State University, Corvallis, Oregon (2011).
[28] A. Kinloch, C. Lau, J. Williams, The peeling of flexible laminates, International Journal of Fracture 66 (1) (1994) 45–70.
[29] Wolfram Research, Mathematica 9.0, Champaign, IL, 2012.
[30] M.-S. Ilvessalo-Pfäffli, Fiber Atlas: Identification of Papermaking Fibers, 1995th Edition, Springer, Heidelberg, Germany, 2011.
[31] J. Bodig, B. A. Jayne, Mechanics of Wood and Wood Composites, Van Nostran-Reinhold Co, Inc., New York, 1982.
[32] Forest Products Laboratory, Wood handbook: wood as an engineering material, General technical report FPL-GTR-190. Madison, WI: U.S. Dept. of Agriculture, Forest Service, 2010.